Dynamics of the double-beam piezo–magneto–elastic nonlinear wind energy harvester exhibiting galloping-based vibration

Dynamics of the double-beam piezo-magneto-elastic nonlinear wind energy harvester exhibiting galloping-based vibration

Junlei Wang[1], Linfeng Geng[1], Kai Yang[2*], Liya Zhao[3], Fei Wang[4], Daniil Yurchenko[5]

1. School of Mechanical and Power Engineering, Zhengzhou University, Zhengzhou 450000, China
2. School of Aerospace Engineering, Huazhong University of Science and Technology, Wuhan 430074, China
3. School of Mechanical and Mechatronic Engineering, Faculty of Engineering and Information Technology, University of Technology Sydney, 15 Broadway, Ultimo 2007, NSW, Australia
4. School of Microelectronics, Southern University of Science and Technology, Shenzhen 518055, China
5. Institute of Mechanical, Process & Energy Engineering, Heriot-Watt University, Edinburgh EH14 4AS, UK

*Corresponding author: Kai Yang, email: kaiyang@hust.edu.cn;

ABSTRACT

This paper investigates a dynamic model and behavior of a novel double-beam piezo-magneto-elastic nonlinear wind energy harvester (DBPME-WEH). The DBPME-WEH is a double-beam structure, which contains the magnet-induced bistable nonlinearity to enhance the performance of the galloping-based vibration energy harvesting. The corresponding governing equations of motion are formulated, and the numerical results based on the equations are validated by a series of the wind tunnel experiments. Both the numerical and experimental results show that the DBPME-WEH outperforms the linear double-beam piezoelectric wind energy harvester, significantly reducing the cut-in speed. To understand the nonlinear dynamic behavior of the proposed energy harvester, this study performs the numerical investigations of the time-domain responses, phase portraits and frequency spectrums of the DBPME-WEH under selected wind speeds. The intra-well, chaotic and inter-well oscillations are discovered with respect to low, medium and high wind speeds intervals respectively. The parametric study is performed to uncover the influences of the beams stiffness ratio, effective mass ratio and the height of the bluff body, that help developing the insights of the effective design of the DBPME-WEH.

Keywords: Energy harvesting; galloping vibration; magnet-induced nonlinearity; bistable; double beam

1 Introduction

In recent years, the technology of environmental energy harvesting has been developing rapidly with the booming of advanced materials and mechanical manufacturing techniques [1-6]. Flow induced vibration energy harvester (FIVEH) is a kind of a micro/macro environmental energy capture device, capable of harvesting marine and wind energy from the environment. It

has been widely studied because of its environmental protection, a relatively simple engineering structure as well as ability to harvesting energy from low-speed flows [7-13].

FIV energy harvesters can be categorized into piezoelectric, magneto-electrics, electrostatic and dielectric energy generators by the energy conversion mechanisms [14-19]. Among them, the piezoelectric energy harvesters (PEH) have been extensively studied for its simple structure and high energy conversion density [20, 21]. Akaydin et al. [22, 23] made a piezoelectric cantilever beam with a piezoelectric material to explore the opportunity of harvesting wind energy from a turbulent boundary layer. The experimental results showed that the output power of the energy harvester was approximately 0.1 mW when the wind speed was 1.192 m/s. The efficiency of the energy harvester was calculated to be 0.72%, and the power density was 233W/m^3 within the operational wind speed range. Abdelkefi et al. [24-26] studied the harvesting of wind energy by transverse galloping. The output power of the energy harvester and the cut-in speed (the lowest wind speed required to activate the galloping vibration) of galloping under different wind speeds and load resistances were investigated. The experimental results showed that the cut-in speed of galloping depends on the load resistances, and there exists an optimum resistance to maximize the output power of the energy harvester. At the same time, the maximum output power is accompanied by the minimum transverse displacement amplitude. Yan et al. [27-29] further studied the influence of the interface circuit (DC circuit, AC circuit and inductance-resistance circuit) on the galloping-based piezoelectric energy harvester. The results showed that the performance of two energy harvesters was with DC circuit and AC circuit almost identical at the low wind speeds because of the same optimal electrical damping, and the energy harvester with AC circuit interface had a higher harvested power with a lower displacement amplitude at the high wind speeds. The energy harvester with the inductance-resistance circuit interface can adjust and realize any optimal electrical damping by in series or parallel the inductance and resistance, improving the performance at the high wind speeds.

In order to improve the efficiency of an energy harvester, Zhang et al. [30, 31] contrasted the influence of the interference cylinders with the different cross sections on the tandem cylinders for improving the operational wind speed range and the cut-in speed of the energy harvester. The experimental results showed that the average output power of the energy harvester with the interference square cylinder reached 803.4 μW at the wind speed of 2.36 m/s, thereby increasing the bandwidth by 380% compared to the energy harvester without the interference cylinder. He et al. [32] and Bibo et al. [33, 34] studied the performance of enhanced wind energy harvesters by coupling a variety of the vibration sources, such as the vortex-induced vibration, galloping and a basic excitation. The results showed that the interaction of various types of vibrations can improve the performance of the wind harvester and its efficiency, as well as the operational wind speed range. Wang et al. [35] studied how to improve the surface structure of a bluff body by using Y-type attachments to improve the performance of the piezoelectric wind energy harvester. Franzini and Bunzel [36] compared the piezoelectric energy harvester with two-degree-of-freedom and single-degree-of-freedom under eddy-induced vibrations. Hu et al. [37] proposed a lumped parameter model describing the coupling of multiple physical fields to

determine the optimal position of the energy harvester in the wake. For a flow-induced vibration piezoelectric energy harvester, the operational wind speed range and output power were the main indicators to evaluate its performance. How to improve the operational wind speed range and output power of the energy harvester is the focus of the current worldwide research on flow-induced vibration energy harvesting.

In the above studies, linear host structures were utilized to transmit the wind energy into the vibrational energy. Recently, various types of nonlinearities were investigated and proved to be beneficial for the performance improvement of the energy harvesting [38-48] and vibration isolation[49-52], especially using the magnet-induced nonlinearity [53-57]. The advantages of some nonlinear effects have also been considered to improve the vibration mitigation performance. For example, Zhou et al. [53] uncovered the advantage of the snap-through responses of the Y-shaped magnet-induced nonlinear structure for the low-speed wind energy harvesting. Bibo et al. [54] found that an appropriate type of magnet-induced nonlinearity is favorable for a single galloping-based wind energy harvester. Alhadidi and Daqaq [55] and Naseer et al. [56, 57] discussed the benefits of the magnet-induced nonlinearity for the wake-galloping wind energy harvesting and vortex-induced energy harvesting, respectively. To theoretically develop the nonlinear features of a galloping-based bistable energy harvester, Alhussein and Daqaq [58] thoroughly investigated the well-escaping phenomenon of a galloping-based bistable energy harvester under the increasing wind speed. They proposed a simple and yet accurate analytical expression to predict the well-escape speed approximately, which has a great potential in uncovering the insights of a galloping-based multi-stable oscillatory system. Inspired by the previous studies of the magnet-induced nonlinearity, the authors have recently proposed a new double-beam piezo-magneto-elastic wind energy harvester (DBPME-WEH), and experimentally investigated its performance in the wind tunnel [59]. In that paper the authors hypothesized that introducing a bistable nonlinearity using a repulsive force of a magnet, attached to each beam of the double-beam structure, would have a beneficial effect on the overall system performance. However, the DBPME-WEH's mathematical model and the dynamic behavior were neither developed nor studied at all. Having successfully validated the proposed idea through a set of wind tunnel tests, the authors have decided to thoroughly study in detail the mechanisms leading to the beneficial effects of the magnet-induced bistability introduced in the proposed structure. Thus, in this paper the authors derive a mathematical model and study numerically the observed experimentally effects in the efforts of predicting the power output of the device. Moreover, the observed earlier voltage jumping-down phenomenon at high wind speeds, noticed experimentally, has also been observed numerically and the reasons behind it are studied, along with a variety of nonlinear dynamic responses of the system, revealing the valuable insights. Through this study, mathematical model of the DBPME-WEH is validated and can be used for developing and designing the new DBPME harvester.

The rest paper is organized as follows. Section 2 presents the schematic of the DBPME-WEH and formulates its mathematical model for galloping-based vibration. In section 3, the study performs numerical comparison between the DBPME-WEH and the linear double-beam

piezoelectric wind energy harvester (DBP-WEH) which doesn't have the magnets, so as to uncover the advantages of the magnet-induced nonlinearity. Afterward, section 4 shows the experimental results which validate the proposed mathematical model. To understand the nonlinear dynamic behaviors of the DBPME-WEH, section 5 shows the time-domain responses, phase portraits and frequency spectrums of the proposed harvester with respect to certain wind speeds. In section 6, parametric studies of the DBPME-WEH are conducted to develop the insights into effective design of the DBPME-WEH. Finally, the main findings are concluded in section 7.

2 Dynamic modeling

2.1 Description of the DBPME-WEH

Figs.1 (a) and (b) present the front and side view of the DBPME-WEH respectively. The DBPME-WEH consists of two piezoelectric cantilever beams (denoted as the 1st beam and 2nd beams, respectively) and two prism-like bluff bodies (denoted as the 1st and 2nd bluff bodies, respectively). The length and width of the *i*th beam are l_{bi} and h_{bi}, respectively. The length and width of the *i*th bluff body are l_i and h_i, respectively, where the bluff body's cross-section is a square (i.e., the area is h_i^2). The tip of each bluff body is embedded with an identical magnet. The two magnets are oriented to repulse each other, which consequently produces magnet-induced nonlinearity. For modeling the magnetic interaction force the dipole model of the two magnets is used in this study. Thus, D is defined as the distance between the two magnetic poles. As shown in Fig. 1(b), when D is smaller than a certain value, the repulsive magnetic force buckles both the beams. Consequently, the bluff body has bi-stable static equilibrium positions which are symmetric about the center line, i.e., bistable nonlinearity. Note that, if the two repulsive magnets are removed, the system becomes a linear double-beam piezoelectric wind energy harvester (DBP-WEH), which is used for comparison in the next section. When the DBPME-WEH is subjected to a wind excitation, the DBPME-WEH's galloping vibration may be activated. The galloping vibration energies of both the 1st and 2nd beams are harvested through the electromechanical transduction of the two piezoelectric transducers, respectively.

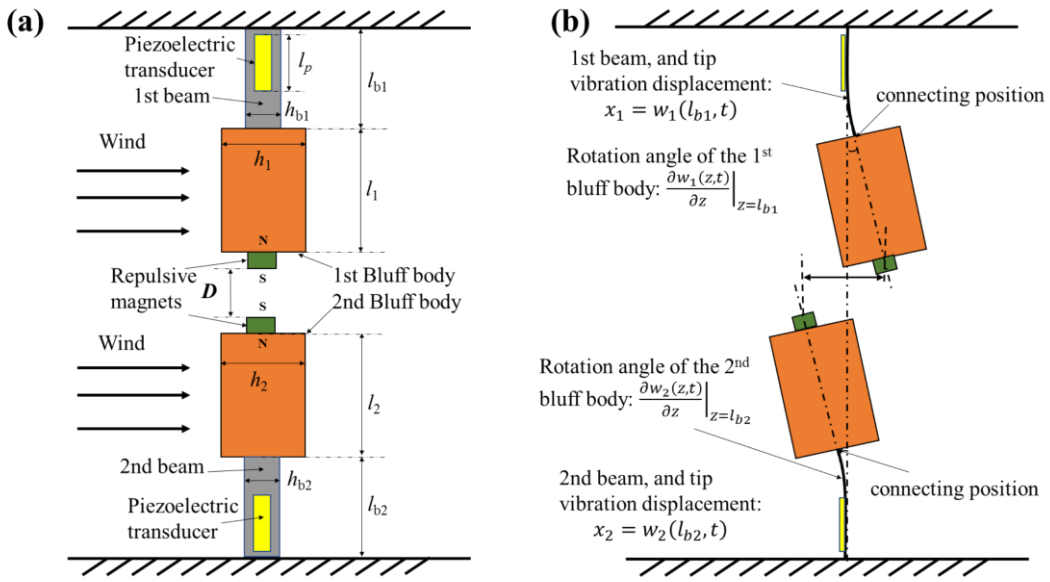

Fig. 1. The schematics of the DBPME-WEH: (a) front view, (b) side view.

2.2 Governing equations

In this study, the beams are made of the same metal material, the bluff bodies are made of the same foam material, and the piezoelectric transducers are identical. Since the length of each beam is far larger than its thickness, Euler-Bernoulli beam theory is used to formulate the vibration of both the beams. In addition, the present study only considers the transverse vibrations of the beams which are significantly greater than the axial tension vibration. As a result, the total kinetic energy of the system T_{total} is expressed as follows,

$$T_{total} = \sum_{i=1}^{2} T_i \tag{1}$$

$$T_i = \frac{1}{2} m_a \left[\left(\frac{\partial w_i(z,t)}{\partial t} + l_i \frac{\partial w_i(z,t)}{\partial z \partial t} \right) \Big|_{z=l_{bi}} \right]^2 + \frac{1}{2} \int_0^{l_i} \rho_g h_i^2 \left[\left(\frac{\partial w_i(z,t)}{\partial t} + s \frac{\partial w_i(z,t)}{\partial z \partial t} \right) \Big|_{z=l_{bi}} \right]^2 \mathrm{d}s + \frac{1}{2} \int_0^{l_{bi}} \rho S_{bi} \left(\frac{\partial w_i(z,t)}{\partial t} \right)^2 \mathrm{d}z \tag{2}$$

where $i = 1,2$ denotes the 1st and 2nd beams, respectively. T_i is the total kinetic energy of the ith beam, ith bluff body and ith magnet, m_a is the mass of the magnet, ρ, ρ_g are the densities of the piezoelectric beam (deemed as a composite structure of the piezoelectric transducer and metal beam) and the bluff body, respectively. S_{bi} is the cross-section areas of the ith beam, s is the coordinate of the bluff body, so $s = 0$ denotes the connecting position of the beam and bluff body (as shown in Fig.1(b)). $w_i(z,t)$ is the transverse displacement of the ith beam at the coordinate z and time t. As shown in Fig. 1 (b), the rotational angle of the ith bluff body is $\partial w_i(z,t)/\partial z|_{z=l_{bi}}$.

Since both the bluff bodies and beams are lightly weighted, the potential energy of the gravity (which is much smaller than the elastic potential energy of the system) is neglected. The potential energy of the system $V_{potential}$ is [20]

$$V_{potential} = \sum_{i=1}^{2} V_i \tag{3}$$

$$V_i = \frac{1}{2}\int_0^{l_{bi}} EI\left(\frac{\partial^2 w_i(z,t)}{\partial z^2}\right)^2 dz - \int_{Z_{pi}}^{Z_{pi}+l_p} J_p v_i \frac{\partial^2 w_i(z,t)}{\partial z^2} dz + \frac{1}{2} C_p v_i^2 \tag{4}$$

where EI is the bending stiffness of the piezoelectric beam, which is related to the Young's modulus and the area moment of inertia of the composite structure of the beam and piezoelectric transducers. v_i is the voltage output of the piezoelectric transducer attached on the *i*th beam. J_p is the electro-mechanical transduction coefficient, which is related to the piezoelectric constant and the volume of the piezoelectric transducer [20]. Z_{pi} is the position of the piezoelectric transducer attached on the *i*th beam, and l_p is the length of the piezoelectric transducer. C_p is the capacitance of the piezoelectric transducer.

The work done by the external forces for small deviation of both the beams are

$$\delta W = \sum_{i=1}^{2} \delta W_{gi} + \delta W_{mag} \tag{5}$$

$$\delta W_{gi} = \int_0^{l_i} F_{gi}(s)\delta\left[(w_i(z,t) + s\frac{\partial w_i(z,t)}{\partial z})\Big|_{z=l_{bi}}\right]\mathrm{d}s \tag{6}$$

$$\delta W_{mag} = -F_{mag}\delta\left(w_1(l_{b1},t) + l_1\frac{\partial w_1(z,t)}{\partial z}\Big|_{z=l_{b1}} - w_2(l_{b2},t) - l_2\frac{\partial w_2(z,t)}{\partial z}\Big|_{z=l_{b2}}\right) \tag{7}$$

where δW_{gi} is the work done of the galloping force $F_{gi}(s)$ of the *i*th bluff body under the galloping excitation. δW_{mag} is the work done of the magnetic force F_{mag}. According to [60] and [61], F_{gi} and F_{mag} are:

$$F_{gi}(s) = \frac{1}{2}\rho_a h_i\left\{A_1 U\left(\frac{\partial w_i(z,t)}{\partial t} + s\frac{\partial w_i(z,t)}{\partial z\partial t}\right)\Big|_{z=l_{bi}} + \frac{A_3}{U}\left[\left(\frac{\partial w_i(z,t)}{\partial t} + s\frac{\partial w_i(z,t)}{\partial z\partial t}\right)\Big|_{z=l_{bi}}\right]^3\right\} \tag{8}$$

$$\begin{aligned} F_{mag} = {} & a\left(w_1(l_{b1},t) + l_1\frac{\partial w_1(z,t)}{\partial z}\Big|_{z=l_{b1}} - w_2(l_{b2},t) - l_2\frac{\partial w_2(z,t)}{\partial z}\Big|_{z=l_{b2}}\right) \\ & + b\left(w_1(l_{b1},t) + l_1\frac{\partial w_1(z,t)}{\partial z}\Big|_{z=l_{b1}} - w_2(l_{b2},t) - l_2\frac{\partial w_2(z,t)}{\partial z}\Big|_{z=l_{b2}}\right)^3 \end{aligned} \tag{9}$$

where ρ_a is the air density. A_1 and A_3 are the empirical coefficients for the aerodynamic force calculation [60]. U is the wind speed, a, b are the coefficients of the magnetic repulsive force which are approximately [61]

$$a = -\frac{12H_0}{D^5} \tag{10}$$

$$b = \frac{45H_0}{D^7} \tag{11}$$

where $H_0 > 0$ is a constant related to the magnetization, volumes of magents and vacuum permeability. It is seen that $a < 0$ and $b > 0$, and they are both decreasing with distance D.

Since the fundamental-mode vibration of the beam is dominant under a wind excitation, the displacement of the *i*th beam $w_i(z,t)$ can be approximately expressed as

$$w_i(z,t) \approx \psi^{(i)}(z)q^{(i)}(t) \tag{12}$$

where $\psi^{(i)}(z)$, $q^{(i)}(t)$ are the fundamental-mode shape function and coordinate of the *i*th beam, respectively. The displacement of the *i*th beam is denoted by $x_i = w_i(l_{bi},t) = \psi^{(i)}(l_{bi})q^{(i)}(t)$. Therefore, Eqs. (1, 3, 5) can be simplified as follows,

$$T_{total} = \sum_{i=1}^{2}\frac{1}{2}M_i\dot{x}_i^2 \tag{13}$$

$$V_{potential} = \sum_{i=1}^{2}(\frac{1}{2}K_i x^2 - \Theta_i x_i v_i - \frac{1}{2}C_p v_i^2) \tag{14}$$

$$\delta W = \sum_{i=1}^{2} F_i \delta x_i \tag{15}$$

where,

$$M_i = m_a\left(1 + \frac{l_i}{\psi^{(i)}(l_{bi})}\frac{\mathrm{d}\psi^{(i)}(z)}{\mathrm{d}z}\Big|_{z=l_{bi}}\right)^2 + \int_0^{l_i}\rho_g h_i^2\left(1 + \frac{s}{\psi^{(i)}(l_{bi})}\frac{\mathrm{d}\psi^{(i)}(z)}{\mathrm{d}z}\Big|_{z=l_{bi}}\right)^2 \mathrm{d}s + \int_0^{l_{bi}}\rho S_{bi}\left(\frac{\psi^{(i)}(z)}{\psi^{(i)}(l_{bi})}\right)^2 \mathrm{d}z \tag{16}$$

$$K_i = \int_0^{l_{bi}} \frac{EI}{\left(\psi^{(i)}(l_{bi})\right)^2}\left(\frac{\mathrm{d}^2\psi^{(i)}(z)}{\mathrm{d}z^2}\right)^2 \mathrm{d}z \tag{17}$$

$$\Theta_i = \int_{Z_{pi}}^{Z_{pi}+l_p} \frac{J_p}{\psi^{(i)}(l_{bi})}\frac{\mathrm{d}^2\psi^{(i)}(z)}{\mathrm{d}z^2}\mathrm{d}z \tag{18}$$

$$F_i = \frac{1}{2}\rho_a h_i\left(\tilde{A}_1^{(i)} U\dot{x}_i + \frac{\tilde{A}_3^{(i)}}{U}\dot{x}_i^3\right) + (-1)^i\lambda_i[a(\lambda_1 x_1 - \lambda_2 x_2) + b(\lambda_1 x_1 - \lambda_2 x_2)^3] \tag{19}$$

$$\tilde{A}_1^{(i)} = \int_0^{l_i}\left(1 + \frac{s}{\psi^{(i)}(l_{bi})}\frac{\mathrm{d}\psi^{(i)}(z)}{\mathrm{d}z}\Big|_{z=l_{bi}}\right)^2 A_1 \mathrm{d}s \tag{20}$$

$$\tilde{A}_3^{(i)} = \int_0^{l_i}\left(1 + \frac{s}{\psi^{(i)}(l_{bi})}\frac{\mathrm{d}\psi^{(i)}(z)}{\mathrm{d}z}\Big|_{z=l_{bi}}\right)^4 A_3 \mathrm{d}s \tag{21}$$

$$\lambda_i = \left(1 + \frac{l_i}{\psi^{(i)}(l_{bi})}\frac{\mathrm{d}\psi^{(i)}(z)}{\mathrm{d}z}\Big|_{z=l_{bi}}\right) \tag{22}$$

Assuming that the *i*th beam has the equivalent mechanical damping C_i for the fundamental-mode vibration, based on the Lagrange equation, the governing equations of the galloping vibrations of the DBPME-WEH are presented as follows:

$$M_1\ddot{x}_1 + \left(C_1 - 0.5\rho_a h_1 \tilde{A}_1^{(1)} U\right)\dot{x}_1 - 0.5\frac{\rho_a h_1 \tilde{A}_3^{(1)}}{U}\dot{x}_1^3 + K_1 x_1 + \lambda_1[a(\lambda_1 x_1 - \lambda_2 x_2) + b(\lambda_1 x_1 - \lambda_2 x_2)^3] - \Theta_1 v_1 = 0 \tag{23}$$

$$M_2\ddot{x}_2 + \left(C_2 - 0.5\rho_a h_2 \tilde{A}_1^{(2)} U\right)\dot{x}_2 - 0.5\frac{\rho_a h_2 \tilde{A}_3^{(2)}}{U}\dot{x}_2^3 + K_2 x_2 - \lambda_2[a(\lambda_1 x_1 - \lambda_2 x_2) + b(\lambda_1 x_1 - \lambda_2 x_2)^3] - \Theta_2 v_2 = 0 \tag{24}$$

When each piezoelectric transducer is connected with a load resistor R_L, the following electric equations can be obtained:

$$C_p\dot{v}_1 + \Theta_1\dot{x}_1 + \frac{v_1}{R_L} = 0 \tag{25}$$

$$C_p\dot{v}_2 + \Theta_2\dot{x}_2 + \frac{v_2}{R_L} = 0 \tag{26}$$

Eqs. (23-26) can be normalized as follows,

$$\ddot{x}_1 + (2\zeta_1\omega_1 - \gamma_1^{(1)})\dot{x}_1 - \gamma_3^{(1)}\dot{x}_1^3 + \omega_1^2 x_1 + \alpha(x_1 - \Gamma x_2) + \beta(x_1 - \Gamma x_2)^3 - \theta_1 v_1 = 0 \tag{27}$$

$$\ddot{x}_2 + (2\zeta_2\omega_1\sqrt{\mu f} - \mu\gamma_1^{(2)})\dot{x}_2 - \mu\gamma_3^{(2)}\dot{x}_2^3 + \mu f\omega_1^2 x_2 - \mu\Gamma\alpha(x_1 - \Gamma x_2) - \mu\Gamma\beta(x_1 - \Gamma x_2)^3 - \mu\theta_2 v_2 = 0 \tag{28}$$

$$\dot{v}_1 + \eta_1\dot{x}_1 + \sigma v_1 = 0 \tag{29}$$

$$\dot{v}_2 + \eta_2\dot{x}_2 + \sigma v_2 = 0 \tag{30}$$

where the definitions of the normalized parameters in the Eqs. (27-30) are listed in Table 1.

Table 1 Definition of the normalized parameters in the governing equations, where $i = 1,2$ denotes the 1st beam and 2nd beam, respectively.

Definition	Parameter
Equivalent natural frequency of the 1st beam	$\omega_1 = \sqrt{K_1/M_1}$
Beam damping ratio	$\zeta_i = C_i/(2\sqrt{M_i K_i})$
Beam stiffness ratio	$f = K_2/K_1$
Length ratio	$\Gamma = \lambda_2/\lambda_1$
Effective mass ratio	$\mu = M_1/M_2$
Normalized coefficient of the magnetic-force linear term	$\alpha = a\lambda_1^2/M_1$
Normalized coefficient of the magnetic-force cubic term	$\beta = b\lambda_1^4/M_1$
Normalized linear aerodynamic damping	$\gamma_1^{(i)} = 0.5\rho_a h_i \tilde{A}_i^{(i)} U/M_1$
Normalized cubic aerodynamic damping	$\gamma_3^{(i)} = 0.5\,\rho_a h_i \tilde{A}_3^{(i)}/M_1 U$
Coupling coefficient normalized by the mass	$\theta_i = \Theta_i/M_1$
Coupling coefficient normalized by the capacitance	$\eta_i = \Theta_i/C_p$
Equivalent impedance	$\sigma = 1/R_L C_p$

By letting the time derivatives in Eqs. (27-30) be zero, the system equilibria can be calculated, which is:

$$\left[x_{eq1}, x_{eq2}, v_{eq1}, v_{eq2}\right] = \begin{cases} [0,0,0,0],\ f^3\omega_1^2 + \alpha f^2(f+\Gamma^2) \geq 0 \\ [\pm\sqrt{-\frac{f^3\omega_1^2+\alpha f^2(f+\Gamma^2)}{\beta(f+\Gamma^2)^3}}, \mp\frac{\Gamma}{f}\sqrt{-\frac{f^3\omega_1^2+\alpha f^2(f+\Gamma^2)}{\beta(f+\Gamma^2)^3}}, 0,0],\ f^3\omega_1^2 + \alpha f^2(f+\Gamma^2) < 0 \end{cases} \quad (31)$$

When $\left[x_{eq1}, x_{eq2}\right] = 0$, the system exhibits monostable nonlinearity; when $\left[x_{eq1}, x_{eq2}\right] \neq 0$, the system exhibits bistable nonlinearity. Since the absolute values of normalized nonlinear stiffness α and β gradually decrease with the increase of the distance D, the equilibrium point will vary greatly with distance D.

By Eqs. (9) and (14), the nonlinear potential energy of both the beams for a static system can be expressed as:

$$E_{potential}^{(i)} = \frac{1}{2}K_i x^2 + \int_0^{x_i} F_{mag}\, dx_i \quad (i = 1,2) \quad (32)$$

Fig.2 shows the variation of the potential energy of the DBPME-WEH's 1st beam as a function of distance *D*. It should be noted that the displacement of the 2nd beam is far less than that of the 1st beam under a low wind speed, thus the influence of the displacement of the 2nd beam on the magnetic force can be temporarily ignored. Results show that the depth of the potential energy well decreases gradually with the increase of distance *D*. When *D* is 12 mm or 15 mm, the DBPME-WEH exhibits a strong bistable nonlinearity, and the well depth are

1.17×10^{-4} and 2.7×10^{-5}, respectively. When D increases to 18 mm, the DBPME-WEH still possesses a weakly bistable nonlinearity. In this case the potential energy well is very shallow, which makes it easy for the bluff body escape from, thus facilitating the bluff body's large inter-well oscillations.

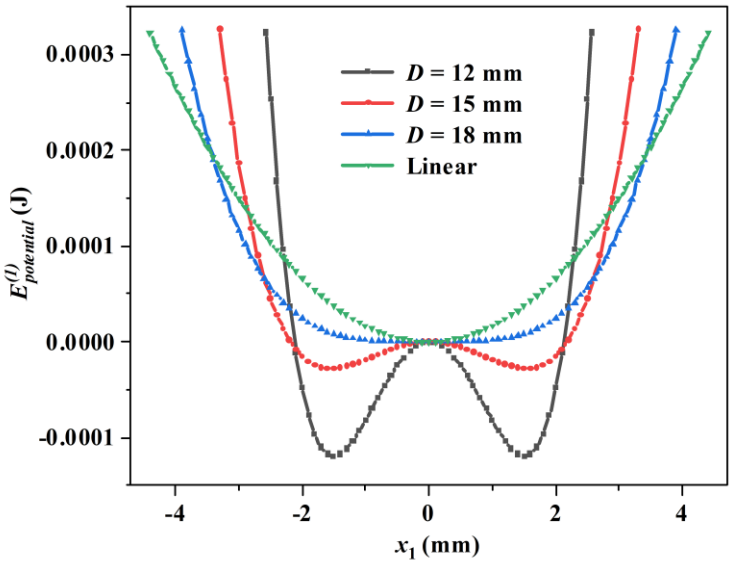

Fig. 2 The potential energy of 1st beam of the DBPME-WEH with respect to x_1 for different distance D

3 Performance comparison and influence of the magnet-induced nonlinearity

3.1 Performance comparison

To show the advantages of the DBPME-WEH, a linear double-beam piezoelectric wind energy harvester (DBP-WEH) is used as a comparative counterpart in this study. By removing the magnets, the DBPME-WEH becomes DBP-WEH. Thus, the governing equations of the DBP-WEH are the special situations of Eqs. (27-30) when $\alpha = 0$ and $\beta = 0$. The simulation parameters are listed in Table 2, which are the rounded values corresponding to the experimentally identified values of the prototype in the next section. The structural parameters $M_{1,2}$, $\omega_{1,2}$, $\zeta_{1,2}$ and $\theta_{1,2}$ were identified by measuring both the vibration displacements and voltage outputs through the free attenuation experiment of each cantilever beam. In the following simulations, the values of the structural parameters were then rounded. For example, the equivalent mass and resonant frequency of the 1st beam were selected to be $M_1 = 0.005$ kg and $\omega_1 = 13$ Hz, respectively. The mass ratio $\mu = M_1/M_2$ and beam stiffness ratio $f = K_2/K_1$ were selected to be 0.9 and 1.6, respectively. The magnet parameters $\alpha_{1,2}$ and $\beta_{1,2}$ were randomly selected values, but they were selected to ensure that the system could exhibit the similar equilibrium positions for the same magnet distance D compared to the experimental protype (i.e. the similar nonlinearity strength). In this section, all the results are obtained by solving the governing equations of the system with 4th-order Runge-Kutta in MALTAB software.

Table 2 The properties of DBPME-WEH

1st beam		2nd beam	
Properties	Value	Properties	Value
M_1	0.005 kg	M_2	0.0056 kg
ω_1	13.0 Hz	ω_2	15.6 Hz
ζ_1	0.015	ζ_2	0.015
λ_1	3.833	λ_2	3.833
α_1	-6.45×10^3	α_2	-6.45×10^3
β_1	1.10×10^9	β_2	1.10×10^9
$\gamma_1^{(1)}$	0.45	$\gamma_1^{(2)}$	0.45
$\gamma_3^{(1)}$	-13.92	$\gamma_3^{(2)}$	-13.92
θ_1	7×10^{-3}	θ_2	7×10^{-3}
η_1	1.73×10^3	η_2	1.73×10^3
σ	384.62	σ	384.62

Figs. 3(a) and (b) show the voltage output standard deviation of the 1st and 2nd beams of the DBPME-WEH and DBP-WEH for wind speeds of 1.5~4.0 m/s. For the DBPME-WEH, the magnet distance $D = 18$ mm. As shown in Fig. 3 (a both the DBPME-WEH and DBP-WEH start to vibrate at the wind speed of 1.9 m/s, and the voltage output increases along with increasing the wind speed. When the wind speed is less than 2.1 m/s, the voltage output of DBPME-WEH is a little lower than that of the DBP-WEH. For wind speed between 2.1~2.9 m/s, the voltage output of the DBPME-WEH is slightly higher than the voltage output of DBP-WEH. For wind speed within 2.9~3.2 m/s, a jumping-down phenomenon can be observed in the voltage output curve of the DBPME-WEH, and the voltage output changes rapidly with the increase of the wind speed. Fig. 3(b) shows that the cut-in speed of DBPME-WEH and DBP-WEH are 1.9 m/s and 2.5 m/s respectively. This indicates that the DBPME-WEH has a wider operational wind speed range than that of the DBP-WEH. For wind speed within 2.1~2.9 m/s interval, the growth trend of the output voltage curve of the DBP-WEH is higher than that of DBPME-WEH. For wind speed 2.9~3.2 m/s, the voltage output curve of the DBPME-WEH can also demonstrate an obvious jumping-down phenomenon similar to Fig. 3(a), and the voltage output of DBPME-WEH is higher than that of DBP-WEH at the wind speed of 3 m/s. When wind speed exceeds 3.2m/s, the DBPME-WEH has a better performance of energy harvesting than the DBP-WEH device.

Note that by comparing both Fig. 3(a) and (b), the cut-in speed of the 2nd beam of DBP-WEH (the counterpart without the nonlinearity) is 2.5 m/s, significantly greater than that of the 1st beam (1.9 m/s) due to the beam stiffness ratio $f = 1.6$ (which means the 2nd beam is much

stiffer than the 1st beam). This can be interpreted by the approximate formula of the cut-in speed given by Tang et al.[60]. The formula shows that it is easier for the softer beam with a bluff body to exhibit the galloping vibration compared to the stiffer beam. However, the 2nd beam of DBPME-WEH can vibrate at a lower wind speed that is close to the cut-in speed of 1st beam due to the interaction of the magnets at the tips of both the bluff bodies. In general, the magnet-induced nonlinearity is beneficial since it enhances the performance of the galloping-based wind energy harvester.

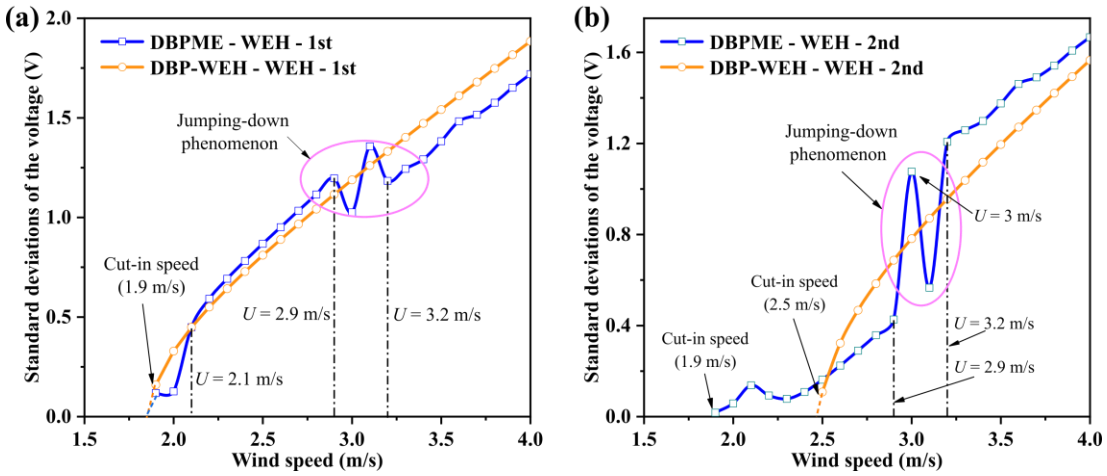

Fig. 3 Numerically predicted comparative results of the voltage output standard deviation of DBPME-WEH and DBP-WEH: (a) 1st beam, (b) 2nd beam.

3.2 Influence of the magnet-induced nonlinearity

As shown in Eqs. (10) and (11), the magnet-induced nonlinearity, which improves the performance of the DBPME-WEH is affected by the distance between the two magnets *D*. Therefore, this subsection explores how the standard deviation of DBPME-WEH voltage output varies as a function of three different distances between the two magnets, so as to uncover the influence of the magnet-induced nonlinearity on the device performance. Fig. 4 shows these results for the 1st and 2nd beams of the DBPME-WEH corresponding to three distances of D = [6, 12, 18] mm. Results indicate that increase in the wind speed can lead to the voltage output improvement of the beams for all the distances D; maximum voltage output of both the beams corresponding to D = 6 mm is significantly lower than that corresponding to D = [12, 18] mm for the maximum wind speed of 4 m/s. It can also be seen that the cut-in speed of the beams decreases with the increase of D. Compared to the cut-in speed of the beams with D = 6 mm, the cut-in speed of the beam with D = 18 mm has decreased by 13.6%. The reason is that when the distance between the magnets is smaller, the nonlinear magnetic force between the two magnets is stronger, and consequently the depth of the potential energy well is greater (as shown in Fig. 2). This leads to the difficulty for both the beams to escape from the potential well to exhibit vibration. In addition, the change of the cut-in speeds of the beams can also be qualitatively interpreted by the formula of the magnet-induced nonlinearity. By Eqs. (9-11), the restoring forces of both beams can be written as:

$$F_1 = K_1 x_1 + K_{b1}(x_1 - x_2) + K_{b3}(x_1 - x_2)^3 \tag{33}$$

$$F_2 = K_2 x_2 + K_{b1}(x_2 - x_1) + K_{b3}(x_2 - x_1)^3 \tag{34}$$

where x_1 and x_2 are the tip displacements of 1st and 2nd bodies, respectively, K_1 and K_3 are the equivalent stiffness of 1st and 2nd beam without magnets respectively. Here, K_{b1} is the negative linear stiffness of the magnet-induced nonlinear force ($K_{b1} = a\lambda_1^2, \lambda_1 = \lambda_2$), and $K_{b1} < 0$, K_{b2} is the positive cubic nonlinear stiffness of magnet-induced nonlinear force ($K_{b3} = b\lambda_1^4, \lambda_1 = \lambda_2$), and $K_{b1} < 0$. Note that, the equivalent total linear stiffness terms of 1st and 2nd beam can be expressed as $(K_1 + K_{b1})$ and $(K_2 + K_{b1})$ respectively, and the negative linear stiffness K_{b1} counterbalances the positive linear stiffness K_i ($i = 1,2$). It can be seen from Eqs. (9) and (10) that the negative linear stiffness K_{b1} decreases when the distance between the magnets D decreases, and thus the total linear stiffness terms $(K_1 + K_{b1})$ and $(K_2 + K_{b1})$ may be of small magnitude for an appropriate distance D.

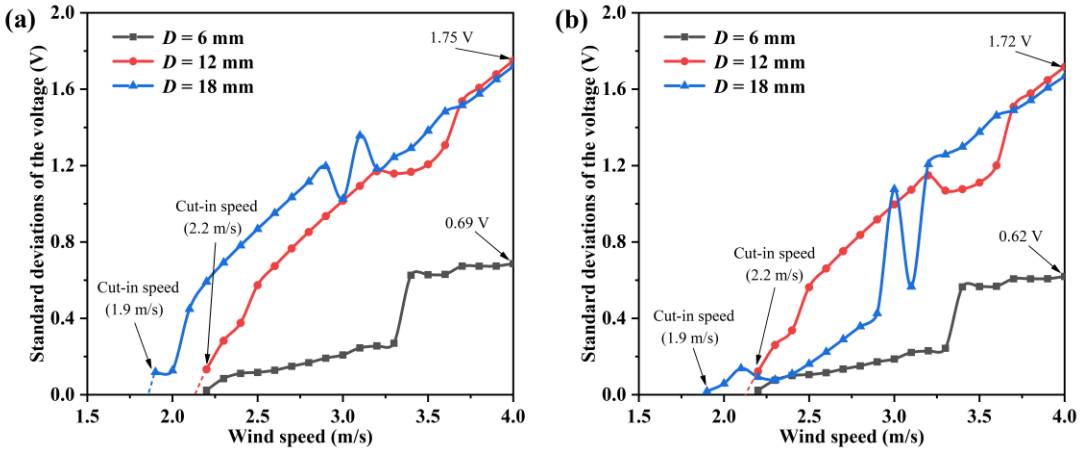

Fig. 4 The numerically predicted voltage output standard deviation of DBPME-WEH with wind speeds and different distance distances of magnets: (a) 1st beam, (b) 2nd beam.

4 Experimental verification

The experimental data presented in the authors' recent work [59] are used to verify the numerical results of DBPME-WEH shown in Figs. 3 and 4. Fig. 5 presents the prototype of the DBPME-WEH prototype installed in the wind tunnel. The prototype consists of two opposite prism-like bluff bodies (material: foam), two piezoelectric cantilever beams (beam material: China GBT 65Mn structural steel; piezoelectric material: PZT-5, capacitance: $C_p = 26$ nF) and an aluminum alloy bracket. A pair of magnets (material: neodymium iron boron, $5 \times 5 \times 5\ mm^3$) are mounted at the bottoms of the bluff bodies. The distance between the two magnets is 18 mm, which can be adjusted by changing the fixed end position of the cantilever beam. The two magnets repulse each other. The total masses of the 1st and 2nd piezoelectric beams are 3.75×10^{-3} kg and 4.65×10^{-3} kg, and the mass of each the bluff body embedded with magnet is 2.72×10^{-3} kg. The geometric parameters of the DBPME-WEH are listed in Table 3. In the experiment, a circular wind tunnel with a diameter of 400 mm is used to provide discrete wind speeds (reserving a decimal fraction): [1.5, 1.7, 1.8, 2.0, 2.1, 2.2, 2.4, 2.5, 2.6, 2.8, 2.9, 3.1, 3.2, 3.3, 3.5,

3.6, 3.7, 3.9] m/s, and the voltage output is measured by a DS1104Z digital oscilloscope (RIGOL Co., China).

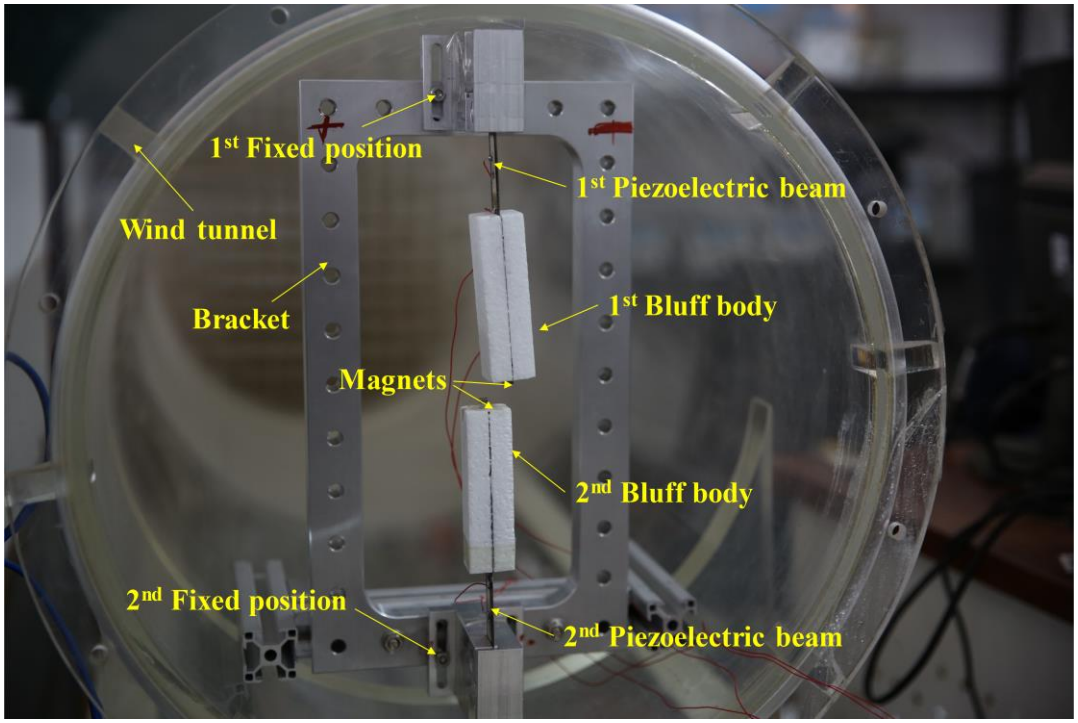

Fig. 5 The prototype of DBPME-WEH in the present work [59]

Table 3 The geometric parameters of the two beams of the DBPME-WEH in the present work [59]

Properties	Value (mm)
1st beam: Length × Width × Thickness	45 × 20 × 0.15
2nd beam: Length × Width × Thickness	45 × 20 × 0.2
1st bluff body: Height × Width × Length	85 × 24 × 24
2nd bluff body: Height × Width × Length	85 × 24 × 24
Piezoelectric transducer: Length × Width × Thickness	30 × 10 × 0.4

The experimental results of the DBPME-WEH and DBP-WEH (by replacing the magnets with the identical mass) obtained in [59] are shown in Fig. 6. Results show that the DBPME-WEH outperform the DBP-WEH in terms of the cut-in wind speeds. The voltage outputs of both harvesters increase along with the increase of the wind speed. For the 1st beam, the cut-in speed of the DBPME-WEH was reduced by 25%; for the 2nd beam the cut-in speed of the DBPME-WEH was reduced by 41.9%. Note that the jumping-down phenomenon of the DBPME-WEH is also discovered in Fig. 6. Thus, the experimental results corroborate the performance improvement and voltage output variations predicted by the numerical simulations (i.e. Fig. 3), regardless of the critical speed variation of the 1st beam. The discrepancy may be interpreted as

follows. The aerodynamic coefficients (A_1 and A_3 in the mathematical model) may vary when the DBPME-WEH was replaced by DBP-WEH in the experiment. Consequently, the cut-in speed of the 1st beam of the DBP-WEH is different from that of the DBPME-WEH. Fig. 7 presents the experimental results of the DBPME-WEH with three different distances: D = [6, 12, 18] mm. Results show that the cut-in speed of the DBPME-WEH decreases with the distance between the magnets D decreases. Compared with the cut-in speed of the DBPME-WEH with D = 6 mm, the cut-in speed of the DBPME-WEH with D = 18 mm decreased by 18%. For the smaller distances of D = 6 mm and D = 12 mm, the cut-in speeds were close. Meanwhile, the voltage output standard deviation of DBPME-WEH with D = 6 mm was significantly lower than that of other groups (D = 12 mm and D = 18 mm). Therefore, the experimental results confirm the influence of the magnet-induced nonlinearity predicted by the numerical simulation on the cut-in speeds and voltage outputs of the DBPME-WEH.

Overall, Figs. 6 and 7 show that both the trends of the numerical and experimental are in good agreement, which validate the mathematical model.

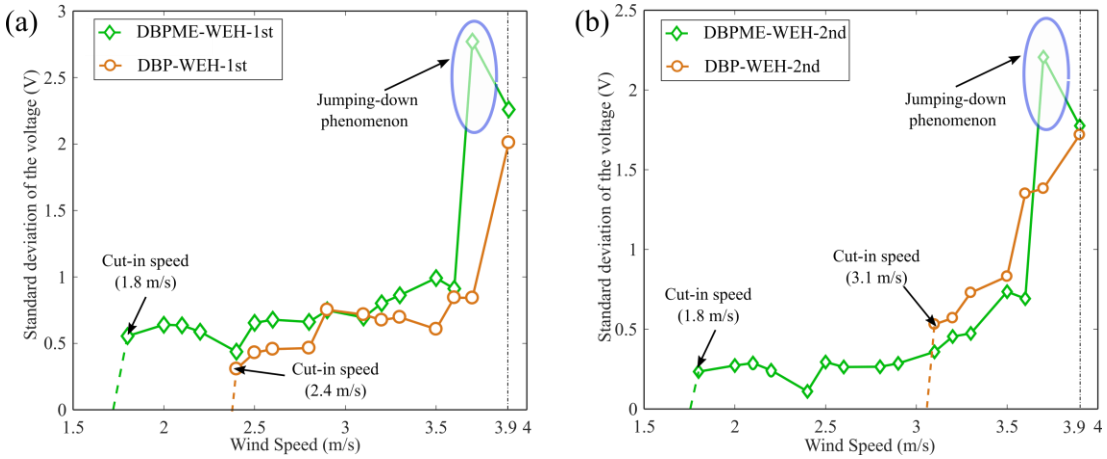

Fig. 6 Comparison of experimental results of DBPME-WEH and DBP-WEH: (a) the voltage output of 1st beam, (b) the voltage output of 2nd beam.

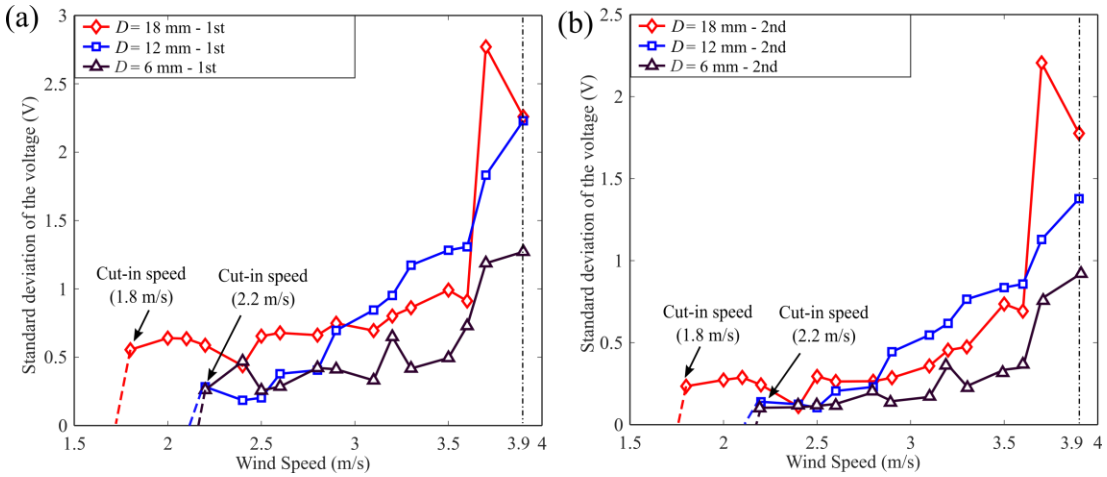

Fig. 7 Comparison of experimental results of DBPME-WEH with different magnet spacing: (a) the voltage output of 1st beam, (b) the voltage output of 2nd beam.

5. Nonlinear dynamic responses of the DBPME-WEH

As shown in Fig. 3, the voltage output trend of the DBPME-WEH varies significantly with the increase of the wind speed, and the vibration states of both the beams change greatly at different wind speeds. This section investigates the nonlinear dynamic responses of the DBPME-WEH in the following two typical wind speed regions: 1.9 ~ 2.1 m/s and 2.9 ~ 3.2 m/s. As shown in Fig.3, the wind speed region of 1.9 ~ 2.1 m/s is in the vicinity of the cut-in speed 1.9 m/s, whereas the wind speed region of 2.9 ~ 3.2 m/s covers the jumping-down phenomenon.

At first, the intra-well responses of the two beams of the DBPME-WEH at low wind speed are presented. Then the chaotic response of the two beams are present. Finally, the periodic inter-well responses of the two beams are compared. The main simulation parameters are as follows: $f = 1.6$, $\mu = 0.9$, $h_1 = h_2 = 0.024$ and D = 18 mm.

5.1 Responses in the vicinity of the cut-in speed 1.9 ~ 2.1 m/s

Figs. 8 (a) and (b) show the dynamic responses of the 1st and 2nd beams for cut-in wind speed U = 1.9 m/s. It is seen that phase portraits of 1st beam has a single closed loop, which surrounds the stable equilibrium position $x_{eq1} = 0.90$ mm. The dominant frequency of the 1st beam's vibration response is 12.7 Hz, which is close to the natural frequency of the beam (13.0 Hz). Therefore, the 1st beam exhibits a periodic intra-well response. Different to the dynamic response of the 1st beams, the vibration response of the 2nd beam is more complex. The phase portrait of the 2nd beam shows that the curves have two closed loops surrounding its stable equilibrium position $x_{eq2} = -0.56$ mm. The FFT results present two dominant frequencies 12.7 Hz and 25.5 Hz. That is, the 2nd beam exhibits period-2 response. On the other hand, the 1st beam's displacement ranges from 0.37 mm to 1.31 mm, producing larger vibration amplitude than that of the 2nd beam (ranges from 0.47 mm to 0.58 mm).

In summary, it is seen that at the cut-in speed 1.9 m/s, the 1st beam of the DBPME-WEH starts vibrating around its equilibrium with a small amplitude due to the small aerodynamic

excitation. For the system without the bistable nonlinearity, Fig.3 shows that the 2nd beam is unable to vibrate at such a speed due to its high stiffness. However, owing to magnetic interaction, the 2nd beam can be also driven to vibrate by the 1st beam once the 1st beam's galloping is activated. Consequently, the 2nd beam also exhibits the small-amplitude intra-well response.

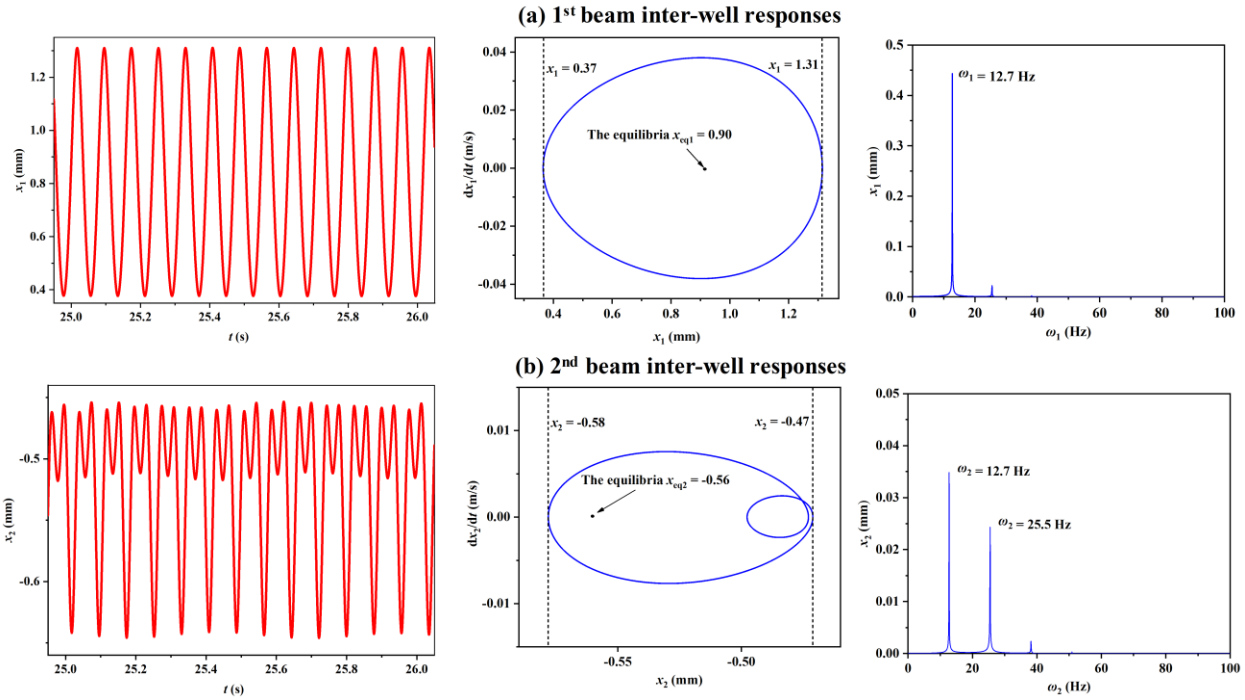

Fig. 8 Time-domain displacement responses plot (left), Phase plot (middle), FFT plot (right) for the **a** 1st beam and **b** 2nd beam under U = 1.9 m/s

With increase of the wind speed, the dynamic responses of both the beams change from periodic intra-well oscillations to the chaotic inter-well oscillations. Fig. 9 shows the time-domain displacement responses, phase portraits and frequency spectrums of both the beams. Results show that for the wind speed U = 2.05 m/s, both the beams exhibit chaotic inter-well responses, which seem to 'randomly' jump from one equilibrium to another. The frequency spectrums of both the 1st and 2nd beams are similar to a stochastic noise's spectrum, showing the dominant frequencies at 11.7 Hz and 14.6 Hz, respectively. In addition, the vibration displacement of the 1st beams ranges from -1.45 mm to 1.45 mm, which is greater than the displacement response of the 2nd beam (-0.93 ~ 0.93 mm).

Fig. 10 compares the phase portraits of the 1st beam for U = [2.0, 2.05, 2.1] m/s. From left to right, along with increase of the wind speeds, the aerodynamic excitation become stronger (i.e. the negative damping term $\gamma_1^{(1)}$ is enhanced). Thus, the 1st beam's behavior changes due to the strongly bistable nonlinearity under the increased of the excitation. The 1st beam experiences the chaotic intra-well oscillations at $U = 2.0$ m/s, chaotic inter-well oscillations at $U = 2.05$ m/s and period-1 inter-well oscillations at $U = 2.1$ m/s. It is seen that the bifurcation occurs between the small-amplitude intra-well oscillation at $U = 2.0$ m/s and large-amplitude inter-well oscillations

at $U = 2.1$ m/s. This is the reason why the voltage output is suddenly increased when the wind speed is changed from 2.0 m/s to 2.1 m/s as shown in Fig. 3(a).

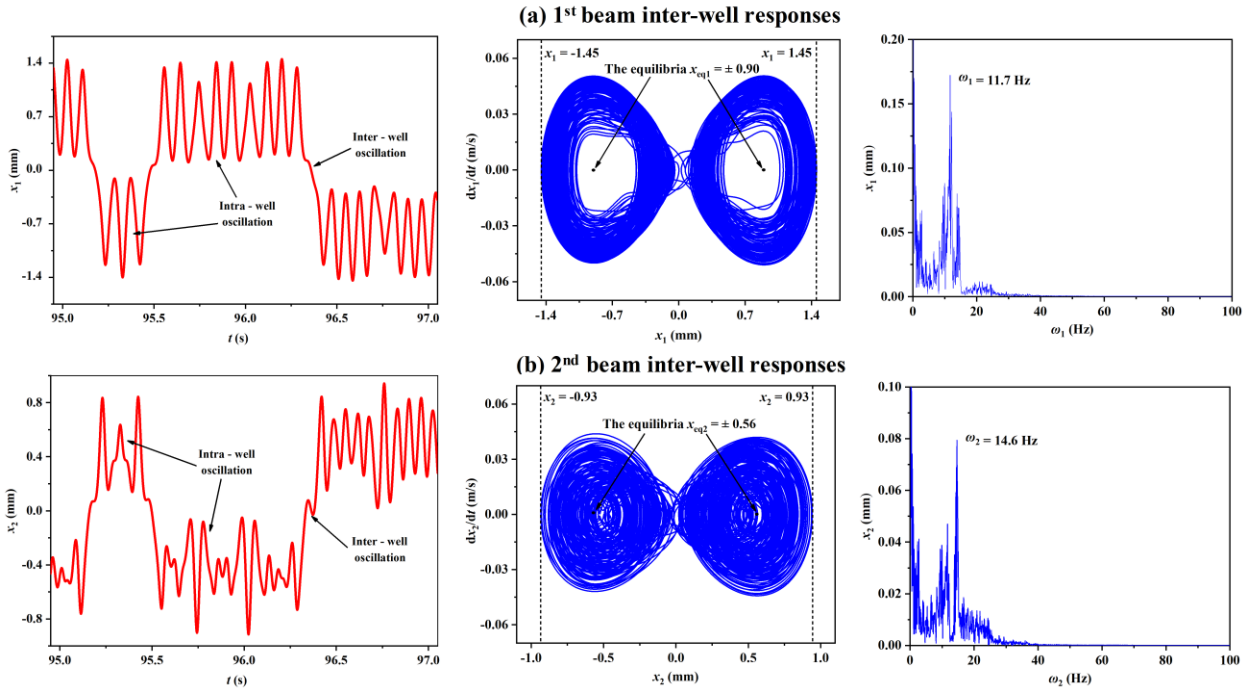

Fig. 9 Time-domain displacement responses plot (left), Phase plot (middle), FFT plot (right) for the **a** 1st beam and **b** 2nd beam under $U = 2.05$ m/s

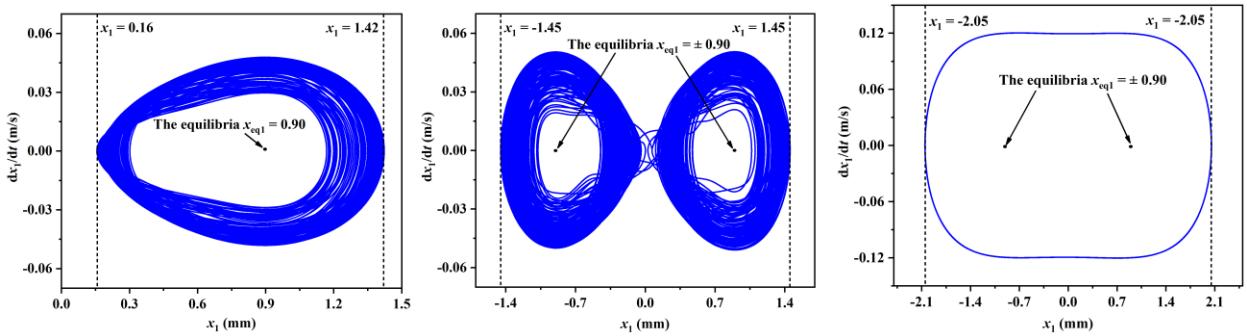

Fig. 10 The phase plot of 1st beam for $U = 2.0$ m/s (left), $U = 2.05$ m/s (middle) and $U = 2.1$ m/s (right)

5.2 Responses in the jumping-down phenomenon area

It can be seen from Fig. 3 that for the wind speed between 2.9 ~ 3.2 m/s, the voltage curve of the DBPME-WEH present a jumping-down phenomenon. In order to analyze the reason behind the jumping-down phenomenon, the time-domain displacement responses, phase portraits and frequency spectrums of the beams for U = [2.9, 3.0, 3.1] m/s are investigated, as shown in Figs. (14-16). Results show that the 1st beam exhibits period-1 inter-well oscillations for $U = 2.9$ m/s. The phase portrait of the beam presents a single closed loop, which surrounds both the equilibrium position $x_{eq1} = \pm 0.90$ mm; the dominant response frequency is 13.8 Hz; the maximum displacement response is 4.60 mm. The dominant response frequency of the 2nd beam is the same as that of the 1st beam, but the maximum displacement of the 2nd beam (1.40 mm) is

smaller than that of the 1st beam. As shown in Fig. 11(b), the FFT plot shows that the superharmonic component (41.4 Hz, which is three times of the dominant frequency component 13.8 Hz) becomes more significant than that in Fig. 11 (a), and consequently the curve's shape of the phase plot is different from that of the 1st beam. At the same time, the comparison of the time-domain displacement responses between both the beams reveals that the phases of the beams are basically the same, which indicates that the periodic oscillations of the two beams are kept synchronous. When U increases to 3.0 m/s, the phases of both the beams are out of phase for nearly half a period, and the dominant response frequencies are close to its doubled value for U = 2.9 m/s. Meanwhile, the displacement response of the 1st beam decreased from 4.60 mm to 2.25 mm, and the displacement of the 2nd beam increased from 1.40 mm to 2.34 mm. Thus, when the wind speed U increases from 2.9 m/s to 3 m/s, the voltage output of the 2nd beam will increase rapidly. When U increases to 3.1 m/s, the phases of both the beams are synchronized again, and the dominant response frequency is reduced to 13.8 Hz. Compared with the displacement response for U = 3.0 m/s, the displacement responses of the beams are changed greatly, and thus the corresponding voltage outputs also vary rapidly with the wind speed. Overall, it can be found that the vibration of each beam changes rapidly along with increasing the wind speed. The jumping-down phenomenon is caused by the phase un-synchronization of both the beams and the magnetic interaction, which causes the response frequencies and displacement responses of the beams to change greatly for some values of the wind speeds.

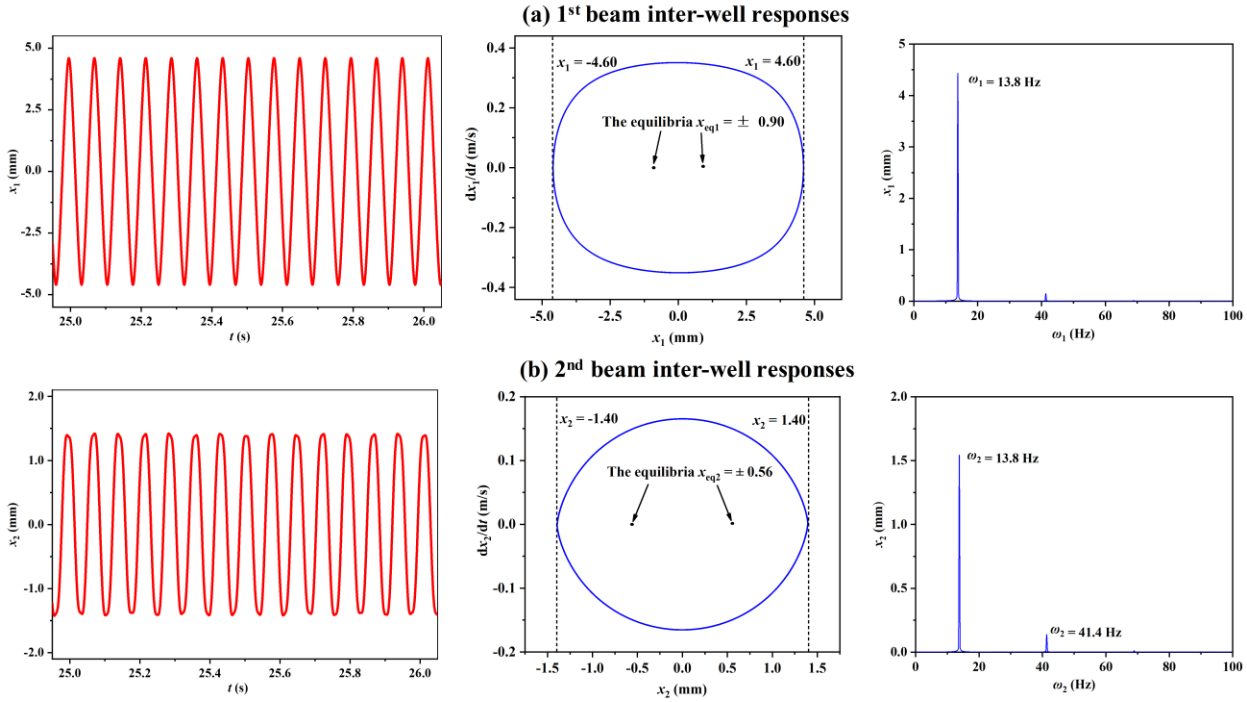

Fig. 11 Time-domain displacement responses plot (left), Phase plot (middle), FFT plot (right) for the **a** 1st beam and **b** 2nd beam under U = 2.9 m/s

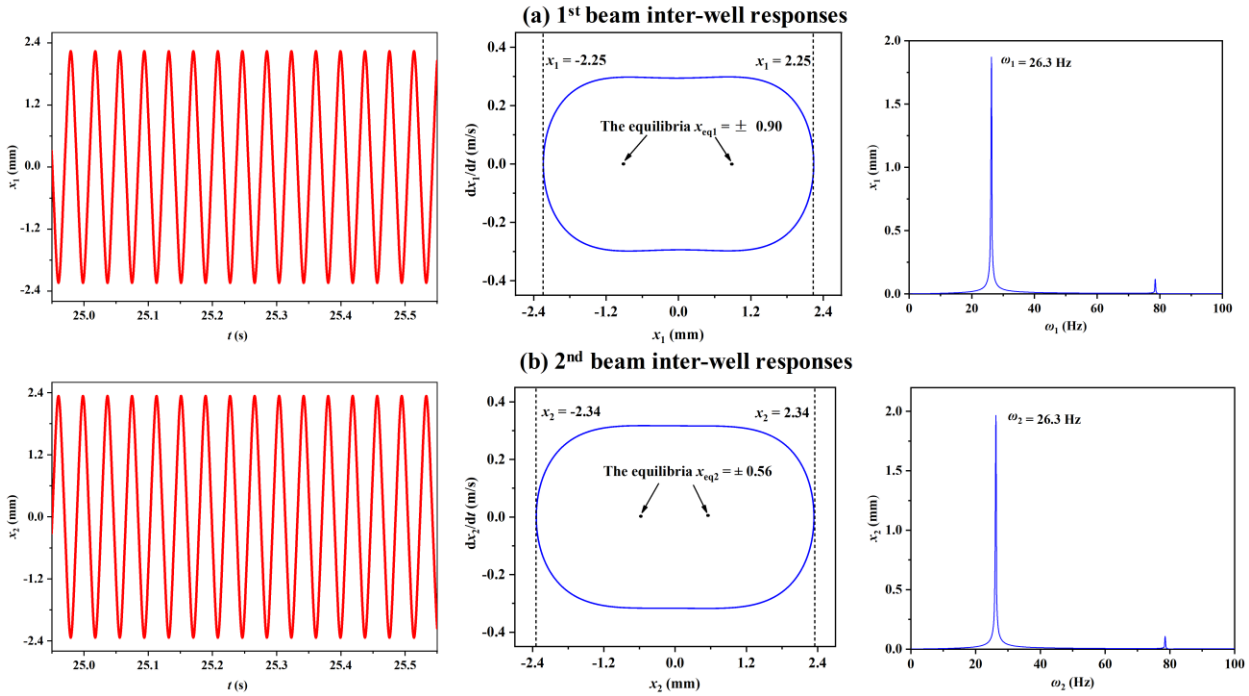

Fig. 12 Time-domain displacement responses plot (left), Phase plot (middle), FFT plot (right) for the **a** 1st beam and **b** 2nd beam under U = 3.0 m/s

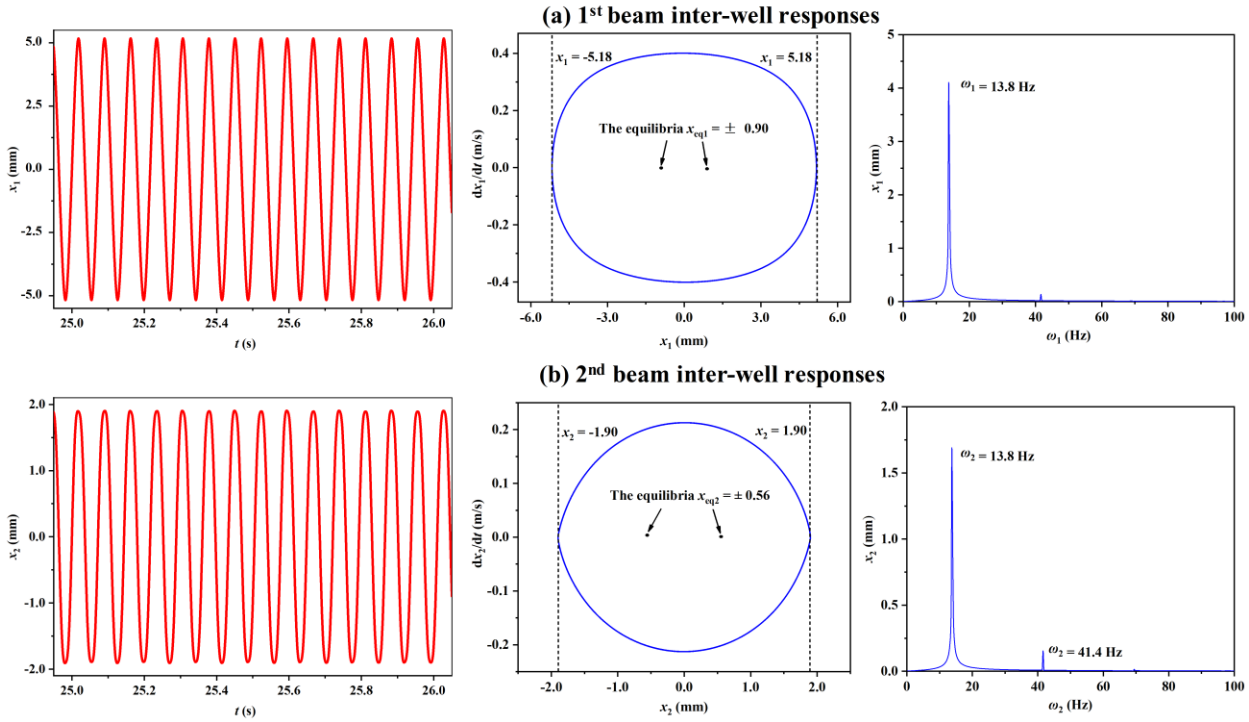

Fig. 13 Time-domain displacement responses plot (left), Phase plot (middle), FFT plot (right) for the **a** 1st beam and **b** 2nd beam under U = 3.1 m/s

6. Parametric study

To develop the insights of the effective DBPME-WEH design, the numerical parametric studies are conducted to investigate the energy harvesting performance of the DBPME-WEH corresponding to the beam stiffness ratio *f*, the effective mass ratio μ and the bluff body widths. The initial numerical simulation parameters are $f = 1.6$, $\mu = 0.9$ and $h_1 = h_2 = h_0 = 0.024$ m. In the following parametric studies, when one parameter changes, other parameters are retained at their initial values, so the 1st beam's effective mass $M_1 = 5 \times 10^{-3}$ kg and equivalent natural frequency $\omega_1 = 2\pi \times 13.0$ rad/s (i.e. 13 Hz) are remained unchanged during the simulation. In the following figures, the wind speed is normalized to be $u^* = U/\omega_1 h_0$ (the non-dimensional form).

6.1 Effects of the beam's stiffness ratio

In order to investigate the influence of the stiffness ratio of the 1st and 2nd beams on DBPME-WEH performance, Fig. 14 presents the voltage output standard deviations of the two beams for the beam stiffness ratio f = [0.5, 1, 2, 4, 6]. Results show that for each *f*, both the beams have the same normalized cut-in speed, and the normalized cut-in speeds change corresponding to the variation of the beam stiffness ratio *f*. As shown in Fig. 14 (a), the normalized cut-in speed for f = 0.5 is 0.82, whereas it increases to 0.97 for f = 1. However, when *f* increases to 2, 4 and 6, the normalized cut-in speed changes slightly. The reason for that is that for f = 0.5, the stiffness of the 2nd beam decreases and is lower than that of the 1st beam (the stiffness of the 1st beam is a given value). Compared with the 1st beam (stiffer beam), 2nd beam (soft beam) is more likely to generate galloping vibration, and then drive the vibration of the 1st beam through the interaction of the magnets at the tips of both the bluff bodies. Thus, the DBPME-WEH with f = 0.5 has a lower cut-in speed. Meanwhile, the maximum voltage outputs of the 1st beams with different beam stiffness ratios are close at the maximum normalized wind speed of 2.0. Different from the variation of voltage output of the 1st beam, when f = 0.5 and 1, the maximum voltage output of the 2nd beam is about 2.06 V at the normalized wind speed of 2.0, which is close to twice the maximum voltage output of the 2nd beam when f = 2, 4 and 6. Therefore, the small stiffness ratio can enhance the performance of the DBPME-WEH.

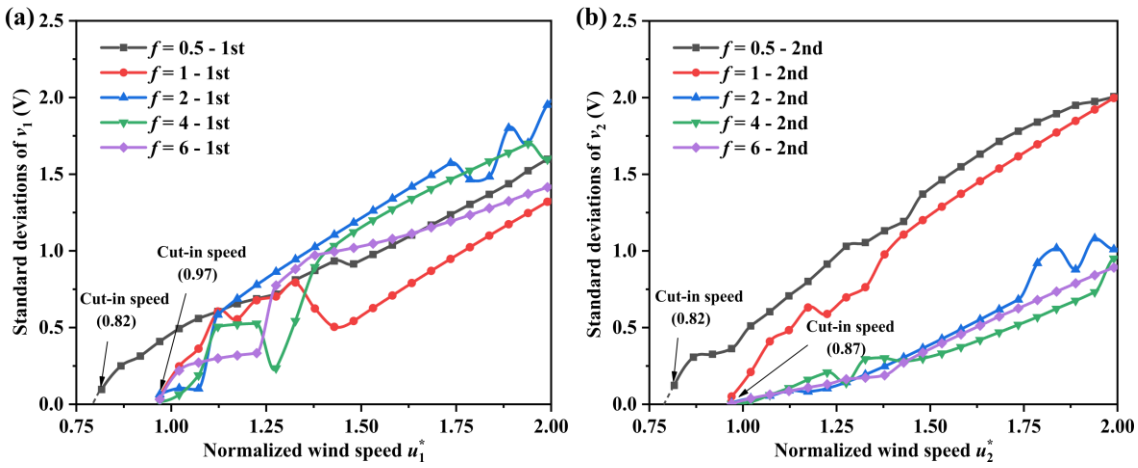

Fig. 14 The voltage output standard deviations of the DBPME-WEH with different stiffness ratios f: (a) 1st beam, (b) 2nd beam, where $u^* = U/\omega_1 h_0$.

6.2 Effects of the effective mass ratio

The voltage outputs of the 1st and the 2nd beams for the effective mass ratios μ = [0.5, 1, 2, 4, 6] are analyzed next to reveal its influence on the galloping vibration. Figs. 15 (a) and (b) show the voltage output standard deviations of two beams under different wind speeds and effective mass ratios, respectively. Results show that the normalized cut-in speed of both the beams changes with increasing μ. For μ = 0.5 and 1, the normalized cut-in speeds of the beams were 0.97. When μ was increased to 2, the normalized cut-in speed of the beams was reduced to 0.87, and when μ increases to 4 and 6, the normalized cut-in speeds of the beams has decreased to 0.61 and 0.51, respectively. The reason is that for the effective mass ratio $\mu > 1$, the cut-in speed of the beams mainly depends on the linear damping term of the 2nd beam ($(2\zeta_2\omega_1\sqrt{\mu f} - \mu\gamma_1^{(2)})\dot{x}_2$). When the damping coefficient ($2\zeta_2\omega_1\sqrt{\mu f} - \mu\gamma_1^{(2)}$) is less than zero, the galloping vibration is generated. At the same time, the absolute values of the damping term $\left|2\zeta_2\omega_1\sqrt{\mu f} - \mu\gamma_1^{(2)}\right|$ rise with the increase of μ, which makes it easier to generate galloping vibration at a lower wind speed. Thus, the cut-in speed of the beams can be reduced by increasing the value of μ. In addition, for μ = [0.5, 1, 2, 4], the voltage outputs of the 1st beam are very close when the normalized wind speed is higher than 1.27, the maximum voltage output is about 1.8 V at the normalized wind speed value 2.0, which is significantly higher than the maximum voltage output for μ = 6. However, the voltage outputs of 2nd beam with μ = 4 and 6 are higher than that of the other three groups. This indicates that for a larger mass ratio, the energy harvesting performance of 2nd beam can be enhanced, but a high mass ratio ($\mu = 6$) may also affect the performance of 1st beam. Overall, for $\mu = 4$, the DBPME-WEH has a better performance.

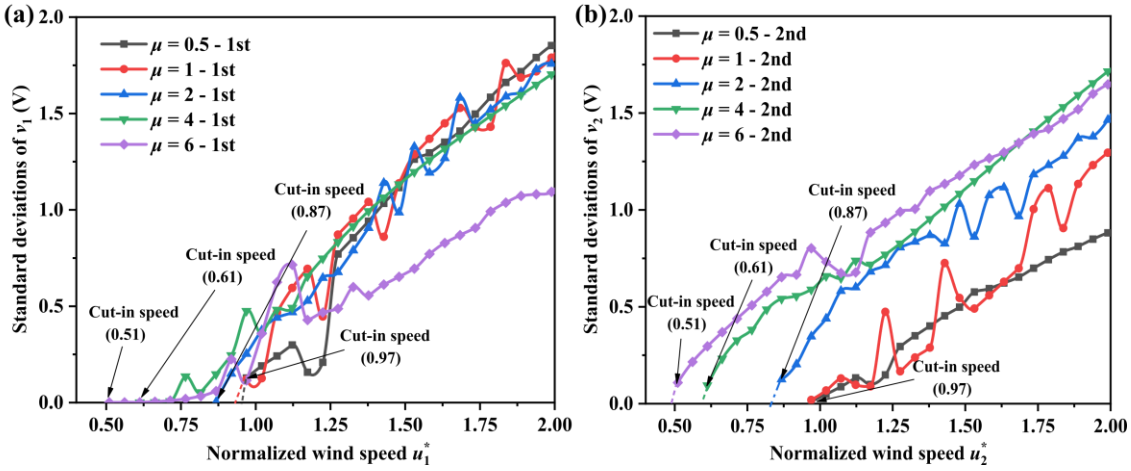

Fig. 15 The voltage output standard deviations of the DBPME-WEH with different mass ratios μ : (a) 1st beam, (b) 2nd beam, where $u^* = U/\omega_1 h_0$.

6.3 Effects of the bluff body width

To uncover the influence of the bluff body width on the DBPME-WEH dynamic behaviors, Fig. 16 shows the voltage output standard deviations of the two beams of the DBPME-WEH for different bluff body widths. In the following simulations, the bluff body widths satisfy $h_1 = h_2 = h^*$, for h^* = [$0.8h_0$, h_0, $2h_0$ $4h_0$, $6h_0$] were selected (where h_0 is the initial bluff body width and size was 0.024 m). By comparing the voltage outputs of the 1st and 2nd beams for different bluff body widths h^* in Figs. 16 (a) and (b), it can be found that the cut-in speeds of the two beams decrease with the increase of h^*. For h^* = $0.8h_0$ and h_0, the normalized cut-in speeds are 1.22 and 0.97, respectively. When h^* increases to $6h_0$, the normalized cut-in speed is reduced to 0.20. It can be seen from Eq. (23) that when the other parameters remain unchanged, the 1st beam's absolute values of the linear aerodynamic damping term $\left|0.5\rho_a h_1 \tilde{A}_1^{(1)} U \dot{x}_1\right|$ and the nonlinear damping term $\left|0.5\frac{\rho_a h_1 \tilde{A}_3^{(1)}}{U}\dot{x}_1^3\right|$ increases with the increase of h^*. When the 1st beam's linear damping coefficient $\left(C_1 - 0.5\rho_a h_1 \tilde{A}_1^{(1)} U\right)$ is reduced to zero, the 1st beam will produce galloping vibrations. At this time, for a larger bluff body width h^*, galloping vibrations are easier to be initiated, which explains why the cut-in speed of the beams decreases with the increase of h*. However, the influence of the nonlinear aerodynamic damping term $\left(0.5\frac{\rho_a h_1 \tilde{A}_3^{(1)}}{U}\dot{x}_1^3\right)$ increases too with the increase of h*, thus the voltage outputs of the beams h* = $4h_0$ and $6h_0$ are close. Therefore, a larger bluff body width can improve the performance of the DBPME-WEH.

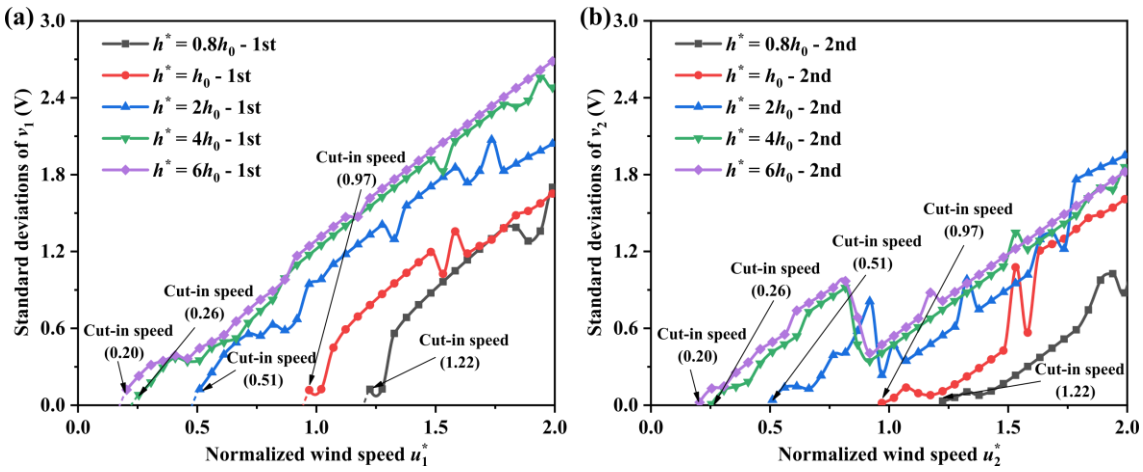

Fig. 16 The voltage output standard deviations of the DBPME-WEH with different the bluff body widths $h_1 = h_2 = h^*$: (a) 1st beam, (b) 2nd beam, where $u^* = U/\omega_1 h_0$.

7 Conclusion

This paper studies the dynamic modeling and nonlinear output response of the DBPME-WEH by developing a mathematical model of the two bluff-body beams interacting through a magnetic repulsive force. Both the numerical and experimental results show that the DBPME-WEH outperforms the DBP-WEH, and the DBPME-WEH significantly reducing the cut-in speed, e.g. 25% reduction in the experiments was observed. Afterward the time-domain responses, phase portraits and frequency spectrums of the DBPME-WEH were investigated to further understand the reasons behind the rich nonlinear dynamics behavior of the device and the variety of the voltage output response curves of both the beams. For wind speeds in the interval of 2.0~2.1 m/s, the 1st beam goes through the chaotic intra-well oscillations, chaotic inter-wells oscillations and periodic inter-wells oscillations, and its displacement response increases rapidly with the wind speed increase. For wind speeds in the range of 2.9~3.2 m/s, both the beams' response demonstrated a jumping-down phenomenon, the response frequencies and displacement responses of the beams changed greatly with the wind increase, which was caused by the phase un-synchronization of both the beams. Finally, the numerically parametric studies were conducted to develop the insights of the effective DBPME-WEH design. The results showed that the performance of the DBPME-WEH can be enhanced by reducing the beam stiffness ratio *f*, selecting an appropriate effective mass ratio ($\mu = 4$) and increasing the bluff body width h^*. However, it was noted that the influence of the bluff body width on the DBPME-WEH performance gradually weakens when the bluff body width increases.

Acknowledgements

This work was supported by National Natural Science Foundation of China (Grant No.: 51977196, 11802097 and 51606171).

Compliance with ethical standards

1. Disclosure of potential conflicts of interest

This work is a foundational research granted by the National Natural Science Foundation of China. The funding information has been presented in the acknowledgements. This work is not used for any commercial business, and thus it has no conflicts of interest.

2. Research involving Human Participants and/or Animals

This work is about the mechanical engineering. This research doesn't involve any human participants or animals.

3. Informed consent

Only the authors listed in the manuscript are involved into this work. The submission of this research is agreed by all the authors listed in the manuscript, and is permitted by both the authors' affiliations.

Reference

[1] H. Liu, J. Zhong, C. Lee, S.-W. Lee, L. Lin, A comprehensive review on piezoelectric energy harvesting technology: Materials, mechanisms, and applications, Applied Physics Reviews, 5 (2018) 041306.

[2] Z. Yang, S. Zhou, J. Zu, D. Inman, High-performance piezoelectric energy harvesters and their applications, Joule, 2 (2018) 642-697.

[3] W. Liu, Z. Yuan, S. Zhang, Q. Zhu, Enhanced broadband generator of dual buckled beams with simultaneous translational and torsional coupling, Applied Energy, 251 (2019) 113412.

[4] Y. Zhang, T. Wang, A. Luo, Y. Hu, X. Li, F. Wang, Micro electrostatic energy harvester with both broad bandwidth and high normalized power density, Applied energy, 212 (2018) 362-371.

[5] M. Gao, J. Cong, J. Xiao, Q. He, S. Li, Y. Wang, Y. Yao, R. Chen, P. Wang, Dynamic modeling and experimental investigation of self-powered sensor nodes for freight rail transport, Applied Energy, 257 (2020) 113969.

[6] Z.-Q. Lu, H. Ding, L.-Q. Chen, Resonance response interaction without internal resonance in vibratory energy harvesting, Mechanical Systems and Signal Processing, 121 (2019) 767-776.

[7] H. Zhu, Y. Zhao, T. Zhou, CFD analysis of energy harvesting from flow induced vibration of a circular cylinder with an attached free-to-rotate pentagram impeller, Applied energy, 212 (2018) 304-321.

[8] Y. Wu, Y. Hu, Z. Huang, C. Lee, F. Wang, Electret-material enhanced triboelectric energy harvesting from air flow for self-powered wireless temperature sensor network, Sensors and Actuators A: Physical, 271 (2018) 364-372.

[9] Y. Ma, Y. Luan, W. Xu, Hydrodynamic features of three equally spaced, long flexible cylinders undergoing flow-induced vibration, European Journal of Mechanics-B/Fluids, 79 (2020) 386-400.

[10] Q. Zou, L. Ding, H. Wang, J. Wang, L. Zhang, Two-degree-of-freedom flow-induced vibration of a rotating circular cylinder, Ocean Engineering, 191 (2019) 106505.

[11] G. Hu, J. Wang, Z. Su, G. Li, H. Peng, K. Kwok, Performance evaluation of twin piezoelectric wind energy harvesters under mutual interference, Applied Physics Letters, 115 (2019) 073901.

[12] L.-C. Zhao, H.-X. Zou, G. Yan, F.-R. Liu, T. Tan, K.-X. Wei, W.-M. Zhang, Magnetic coupling and flextensional amplification mechanisms for high-robustness ambient wind energy harvesting, Energy Conversion and Management, 201 (2019) 112166.

[13] U. Javed, A. Abdelkefi, Characteristics and comparative analysis of piezoelectric-electromagnetic energy harvesters from vortex-induced oscillations, Nonlinear Dynamics, 95 (2019) 3309-3333.

[14] Z. Lai, J. Wang, C. Zhang, G. Zhang, D. Yurchenko, Harvest wind energy from a vibro-impact DEG embedded into a bluff body, Energy Conversion and Management, 199 (2019) 111993.
[15] L.-C. Zhao, H.-X. Zou, G. Yan, F.-R. Liu, T. Tan, W.-M. Zhang, Z.-K. Peng, G. Meng, A water-proof magnetically coupled piezoelectric-electromagnetic hybrid wind energy harvester, Applied Energy, 239 (2019) 735-746.
[16] J. Wang, L. Tang, L. Zhao, Z. Zhang, Efficiency investigation on energy harvesting from airflows in HVAC system based on galloping of isosceles triangle sectioned bluff bodies, Energy, 172 (2019) 1066-1078.
[17] X. Shan, H. Tian, D. Chen, T. Xie, A curved panel energy harvester for aeroelastic vibration, Applied Energy, 249 (2019) 58-66.
[18] J. Wang, G. Hu, Z. Su, G. Li, W. Zhao, L. Tang, L. Zhao, A cross-coupled dual-beam for multi-directional energy harvesting from vortex induced vibrations, Smart Materials and Structures, (2019).
[19] M.F. Daqaq, A. Bibo, I. Akhtar, A.H. Alhadidi, M. Panyam, B. Caldwell, J. Noel, Micropower generation using cross-flow instabilities: a review of the literature and its implications, Journal of Vibration and Acoustics, 141 (2019) 030801.
[20] A. Erturk, D.J. Inman, Piezoelectric energy harvesting, John Wiley & Sons, 2011.
[21] Z.-Q. Lu, J. Chen, H. Ding, L.-Q. Chen, Two-span piezoelectric beam energy harvesting, International Journal of Mechanical Sciences, (2020) 105532.
[22] H.D. Akaydin, N. Elvin, Y. Andreopoulos, Energy harvesting from highly unsteady fluid flows using piezoelectric materials, Journal of Intelligent Material Systems and Structures, 21 (2010) 1263-1278.
[23] H. Akaydin, N. Elvin, Y. Andreopoulos, The performance of a self-excited fluidic energy harvester, Smart materials and Structures, 21 (2012) 025007.
[24] A. Abdelkefi, M.R. Hajj, A.H. Nayfeh, Power harvesting from transverse galloping of square cylinder, Nonlinear Dynamics, 70 (2012) 1355-1363.
[25] A. Abdelkefi, Z. Yan, M.R. Hajj, Modeling and nonlinear analysis of piezoelectric energy harvesting from transverse galloping, Smart materials and Structures, 22 (2013) 025016.
[26] A. Abdelkefi, Z. Yan, M.R. Hajj, Performance analysis of galloping-based piezoaeroelastic energy harvesters with different cross-section geometries, Journal of Intelligent Material Systems and Structures, 25 (2014) 246-256.
[27] T. Tan, Z. Yan, H. Lei, Optimization and performance comparison for galloping-based piezoelectric energy harvesters with alternating-current and direct-current interface circuits, Smart Materials and Structures, 26 (2017) 075007.
[28] Z. Yan, W. Sun, T. Tan, W. Huang, Nonlinear analysis of galloping piezoelectric energy harvesters with inductive-resistive circuits for boundaries of analytical solutions, Communications in Nonlinear Science and Numerical Simulation, 62 (2018) 90-116.
[29] T. Tan, Z. Yan, Electromechanical decoupled model for cantilever-beam piezoelectric energy harvesters with inductive-resistive circuits and its application in galloping mode, Smart Materials and Structures, 26 (2017) 035062.
[30] L. Zhang, H. Dai, A. Abdelkefi, L. Wang, Improving the performance of aeroelastic energy harvesters by an interference cylinder, Applied Physics Letters, 111 (2017) 073904.
[31] L. Zhang, H. Dai, A. Abdelkefi, L. Wang, Experimental investigation of aerodynamic energy harvester with different interference cylinder cross-sections, Energy, 167 (2019) 970-981.
[32] X. He, X. Yang, S. Jiang, Enhancement of wind energy harvesting by interaction between vortex-induced vibration and galloping, Applied Physics Letters, 112 (2018) 033901.
[33] A. Bibo, M. Daqaq, Investigation of concurrent energy harvesting from ambient vibrations and wind using a single piezoelectric generator, Applied Physics Letters, 102 (2013) 243904.
[34] A. Bibo, A. Abdelkefi, M.F. Daqaq, Modeling and characterization of a piezoelectric energy harvester under combined aerodynamic and base excitations, Journal of Vibration and Acoustics, 137 (2015) 031017.
[35] J. Wang, S. Zhou, Z. Zhang, D. Yurchenko, High-performance piezoelectric wind energy harvester with Y-shaped attachments, Energy conversion and management, 181 (2019) 645-652.

[36] G.R. Franzini, L.O. Bunzel, A numerical investigation on piezoelectric energy harvesting from Vortex-Induced Vibrations with one and two degrees of freedom, Journal of Fluids and Structures, 77 (2018) 196-212.
[37] Y. Hu, B. Yang, X. Chen, X. Wang, J. Liu, Modeling and experimental study of a piezoelectric energy harvester from vortex shedding-induced vibration, Energy conversion and management, 162 (2018) 145-158.
[38] K. Yang, F. Fei, H. An, Investigation of coupled lever-bistable nonlinear energy harvesters for enhancement of inter-well dynamic response, Nonlinear Dynamics, 96 (2019) 2369-2392.
[39] K. Yang, Q. Zhou, Robust optimization of a dual-stage bistable nonlinear vibration energy harvester considering parametric uncertainties, Smart Materials and Structures, 28 (2019) 115018.
[40] S. Zhou, L. Zuo, Nonlinear dynamic analysis of asymmetric tristable energy harvesters for enhanced energy harvesting, Communications in Nonlinear Science and Numerical Simulation, 61 (2018) 271-284.
[41] S. Zhou, J. Cao, G. Litak, J. Lin, Numerical analysis and experimental verification of broadband tristable energy harvesters, Tm-Technisches Messen, 85 (2018) 521-532.
[42] Z. Yang, L. Tang, M. Xie, S. Sun, W. Li, K. Aw, Soft magneto-sensitive elastomer and polyvinylidene fluoride polymer based nonlinear piezoelectric energy harvesting: design, modelling and experiment, Smart Materials and Structures, 28 (2018) 015031.
[43] H.-X. Zou, W.-M. Zhang, W.-B. Li, K.-X. Wei, K.-M. Hu, Z.-K. Peng, G. Meng, Magnetically coupled flextensional transducer for wideband vibration energy harvesting: design, modeling and experiments, Journal of Sound and Vibration, 416 (2018) 55-79.
[44] X. Guo, Y. Zhang, K. Fan, C. Lee, F. Wang, A comprehensive study of non-linear air damping and "pull-in" effects on the electrostatic energy harvesters, Energy Conversion and Management, (2019) 112264.
[45] G. Thomson, Z. Lai, D.V. Val, D. Yurchenko, Advantages of nonlinear energy harvesting with dielectric elastomers, Journal of Sound and Vibration, 442 (2019) 167-182.
[46] Z. Yang, L. Tang, K. Tao, K. Aw, A broadband electret-based vibrational energy harvester using soft magneto-sensitive elastomer with asymmetrical frequency response profile, Smart Materials and Structures, 28 (2019) 10LT02.
[47] G. Wang, W.-H. Liao, Z. Zhao, J. Tan, S. Cui, H. Wu, W. Wang, Nonlinear magnetic force and dynamic characteristics of a tri-stable piezoelectric energy harvester, Nonlinear Dynamics, 97 (2019) 2371-2397.
[48] M.F. Daqaq, On intentional introduction of stiffness nonlinearities for energy harvesting under white Gaussian excitations, Nonlinear Dynamics, 69 (2012) 1063-1079.
[49] B. Yan, H. Ma, L. Zhang, W. Zheng, K. Wang, C. Wu, A bistable vibration isolator with nonlinear electromagnetic shunt damping, Mechanical Systems and Signal Processing, 136 (2020) 106504.
[50] B. Yan, H. Ma, W. Zheng, B. Jian, K. Wang, C. Wu, Nonlinear electromagnetic shunt damping for nonlinear vibration isolators, IEEE/ASME Transactions on Mechatronics, 24 (2019) 1851-1860.
[51] B. Yan, H. Ma, B. Jian, K. Wang, C. Wu, Nonlinear dynamics analysis of a bi-state nonlinear vibration isolator with symmetric permanent magnets, Nonlinear Dynamics, 97 (2019) 2499-2519.
[52] K. Yang, R. Harne, K. Wang, H. Huang, Investigation of a bistable dual-stage vibration isolator under harmonic excitation, Smart materials and structures, 23 (2014) 045033.
[53] Z. Zhou, W. Qin, P. Zhu, S. Shang, Scavenging wind energy by a Y-shaped bi-stable energy harvester with curved wings, Energy, 153 (2018) 400-412.
[54] A. Bibo, A.H. Alhadidi, M.F. Daqaq, Exploiting a nonlinear restoring force to improve the performance of flow energy harvesters, Journal of Applied Physics, 117 (2015) 045103.
[55] A. Alhadidi, M. Daqaq, A broadband bi-stable flow energy harvester based on the wake-galloping phenomenon, Applied Physics Letters, 109 (2016) 033904.
[56] R. Naseer, H. Dai, A. Abdelkefi, L. Wang, Piezomagnetoelastic energy harvesting from vortex-induced vibrations using monostable characteristics, Applied Energy, 203 (2017) 142-153.
[57] R. Naseer, H. Dai, A. Abdelkefi, L. Wang, Comparative Study of Piezoelectric Vortex-Induced Vibration-Based Energy Harvesters with Multi-Stability Characteristics, Energies, 13 (2019) 1-24.

[58] H. Alhussein, M.F. Daqaq, Potential well escape in a galloping twin-well oscillator, Nonlinear Dynamics, 99 (2020) 57-72.
[59] K. Yang, J. Wang, D. Yurchenko, A double-beam piezo-magneto-elastic wind energy harvester for improving the galloping-based energy harvesting, Applied Physics Letters, 115 (2019) 193901.
[60] L. Tang, L. Zhao, Y. Yang, E. Lefeuvre, Equivalent circuit representation and analysis of galloping-based wind energy harvesting, IEEE/ASME Transactions on Mechatronics, 20 (2014) 834-844.
[61] C. Lan, L. Tang, W. Qin, L. Xiong, Magnetically coupled dual-beam energy harvester: benefit and trade-off, Journal of Intelligent Material Systems and Structures, 29 (2018) 1216-1235.